Numerical Scale-Up Study for Orthokinetic Agglomeration in Stirred Vessels

E. D. Hollander
Laboratory for Process Equipment and Kramers Laboratorium voor Fysische Technologie, Delft University of Technology, 2628 BW Delft, The Netherlands

J. J. Derksen, L. M. Portela, and H. E. A. Van den Akker
Kramers Laboratorium voor Fysische Technologie, Delft University of Technology, 2628 BW Delft, The Netherlands

Scale-up of orthokinetic agglomeration in stirred-tank reactors was studied numerically. A computer code based on the lattice-Boltzmann method was used to perform large eddy simulations. To account for the dependence of agglomeration on hydrodynamics, the kinetic relation proposed by Mumtaz et al. was applied locally. The convection-reaction equation governing the evolution of the particle-number concentration was solved at the same resolution as the flow field. Three scale-up rules were studied: scale-up at constant Re-number, constant specific power input, and constant impeller tip speed. Vessel sizes varying from 1 to 10,000 L were simulated. The use of two types of impellers (Rushton turbine and Pitched Blade turbine) allowed for investigating the dependence of agglomeration on the macroscopic flow pattern in a reactor. Inhomogeneities in stirred-tank flow caused unpredictable scale-up behavior. Scale-up at constant power input yielded the most constant reactor performance. Impeller geometry had a drastic impact on the observed agglomeration rate, even if the difference in Po number was taken into account.

Introduction

Particle agglomeration is a secondary process frequently encountered in precipitating systems. Primary particles collide in a supersaturated environment, cement together, and form an agglomerate. This mechanism strongly affects the particle size distribution (PSD), since every agglomeration event shifts the PSD towards larger particles. The product properties specified in a particular production process prescribe whether agglomeration should be enhanced or suppressed. For the synthesis of, for example, $Al(OH)_3$ (one of the process steps in the Bayer process), large particle sizes are required to facilitate the solid-liquid separation step in the downstream processing. In this case, agglomeration can be used to increase the apparent growth rate of the material. In manufacturing pigments and dyes, however, a large surface area combined with a high monodispersity of the crystals is needed. In this case, agglomeration should be avoided since it deteriorates the desired properties of the PSD.

Correspondence concerning this article should be addressed to J. J. Derksen.

Increasing demands on product quality, along with stricter environmental constraints, have resulted in a need for a better reactor design. As a consequence, in precipitator design, a shift from reactor models based on ideally stirred tanks (mixed suspension mixed product removal (MSMPR) models (Randolph and Larson, 1971)) toward models based on detailed computational fluid dynamics (CFD) can be witnessed (Leeuwen, 1998; Zauner and Jones, 2000). Incorporation of detailed flow information has shown to give insight in reactor performance (Hollander et al., 2001; Ten Cate et al., 2000).

In this study, we focus on modeling an agglomeration of particles with a size of $\mathcal{O}$ (10 μm). The major difficulty in modeling the process is the fact that agglomeration is the result of three steps (that is, collision, cementation, and possible rupture, see Figure 1) that are intrinsically linked to nonlinear mechanisms like fluid flow and crystal growth. For the particle size studied, the collision step is dominated by velocity gradients in the fluid. Since precipitation reactions are usually performed in stirred vessels, operated in the tur-

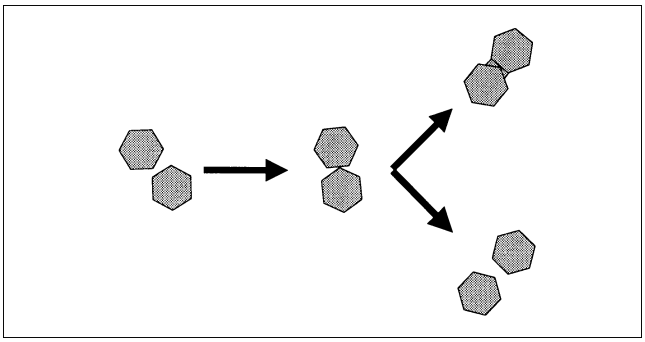

Figure 1. Agglomeration mechanism.

The mechanism consists of a collision step, a cementing step and an effectivity step.

bulent regime, the collision rate is strongly related to the three-dimensional (3-D), transient flow field. The nonlinearities in the governing equations for fluid flow are obvious. The efficiency of a collision is given by both chemical parameters (such as supersaturation) and physical parameters (such as contact time, viscous forces acting on the newly formed agglomerates). Furthermore, crystal morphology and particle size may have an impact on the agglomeration rate. Finally, agglomeration is an intrinsic second-order reaction in particle-number concentration. As a result, models based on (volume) averaged data for the flow field, particle concentration and energy dissipation rate are principally unfit to represent the complex interactions sketched above.

The objective of this article is to investigate the consequences of this nonlinear behavior, by studying scale-up of agglomerators numerically. Reactor performance of 1, 10, 100, 1,000, and 10,000 L vessels, equipped with either a Rushton turbine or a pitched blade turbine, are simulated. For scale-up, three common engineering rules are used, being scale-up at constant *Re*-number, scale-up at constant impeller tip speed, and scale-up at constant mean energy dissipation rate. The flow solver used is based on a lattice-Boltzmann (lB) scheme (Derksen and Van den Akker, 1999). A standard Smagorinsky model is incorporated in the solver to be able to do large eddy simulations (LES) for high Reynolds number simulations. The flow field dependence of the agglomeration rate constant is incorporated by making use of the kinetic relation first proposed by Mumtaz et al. (1997). They numerically derived an expression for the agglomeration rate constant as a function of shear rate in a 2-D planar shear flow. The local hydrodynamic conditions extracted from the flow simulations are translated to an equivalent 2-D shear rate that is subsequently used to estimate the local instantaneous agglomeration rate constant β_0.

For determining the local particle concentration, a scalar transport equation is solved by means of a finite difference technique. Particles are transported by the resolved flow field (that is, particle dispersion due to sub-grid-scale (SGS) motion is ignored). The agglomeration rate is determined from the local particle concentration and the local β_0. This local β_0 is derived from both resolved and SGS flow information. In Hollander et al. (2001), it was shown that agglomeration is particularly sensitive to the small-scale hydrodynamic conditions. Therefore, no compartmentization strategy is used to reduce the number of cells in which the agglomeration process takes place: agglomeration is handled at the same resolution as the flow.

The theoretical aspects of this work are outlined. Issues regarding the implementation of agglomeration in LES-simulations are discussed in detail and the numerical setup for the simulations is described. The results are presented and conclusions are drawn.

Theory

Agglomeration kinetics

Several studies have been published in the literature that model agglomeration in stirred vessels (Van Leeuwen et al., 1998; Bramley et al., 1997; Collier and Hounslow, 1999). The agglomeration rate constant is usually interpreted in terms of the collision rate as derived by Von Smoluchowski (1917). He derived in 1917, for a 2-D shear flow, the collision rate as a function of the shear rate:

$$r_{12} = -\beta_c N_1 N_2 \tag{1a}$$

$$\beta_c = \frac{1}{6}\dot{\gamma}(d_1 + d_2)^3 \tag{1b}$$

The collision rate constant reduces to $\beta_c = 4/3\dot{\gamma}d^3$ for monodisperse particles. Relation 1b shows that the collision rate is proportional to the applied shear rate. It is, however, clear from experiments that this relation is unable to predict agglomeration at high shear rates.

Equation 1b predicts infinite agglomeration rates at infinite shear rates, while experiments indicate that at high shear rates, the agglomeration rate falls to zero. At increasing shear rates, the total number of collisions increases. However, the contact time between the particles decreases and the viscous forces on the freshly formed agglomerates increases. As a consequence, the effectivity of a collision, and, hence, the agglomeration rate, decreases.

The interpretation of experimental agglomeration data obtained in STRs is difficult due to the oversimplification of the flow. For $\dot{\gamma}$ in Eq. 1b, usually a relation like

$$\dot{\gamma} = \sqrt{\frac{\bar{\epsilon}}{\nu}} \propto \sqrt{\frac{PoN^3D^2}{\nu}} \tag{2}$$

is used. In this equation, an intrinsic volume averaging procedure is applied. However, stirred tank flow is not homogeneous. The turbulent energy dissipation rate is an especially strong function of the position in the tank. While ϵ in the impeller region is 10 to 100 times the average dissipation rate in the bulk region ϵ can be orders of magnitude lower than the average dissipation rate. This inhomogeneity makes it virtually impossible to extract correct values for the agglomeration rate constant from stirred tank experiments.

The first article that investigated the effectivity of a collision was based on a numerical study by Mumtaz et al. (1997). In that work, the interfaces of two particles moving in a 2-D

simple shear flow are tracked. The interfaces grow due to the fact that a supersaturated environment is applied. When the interfaces touch, crystal growth forms a bond between the interfaces. If the strength of the bond is larger than that of the viscous forces acting on the agglomerate, the collision is assumed to be successful; otherwise, the collision is ineffective. By repeating the experiment with different shear rates and approach angles, the average agglomeration rate constant as a function of shear rate was constructed. The shear rate dependence of β_0 is shown in Figure 2. These kinetics will be used in this article.

The use of this kinetic relation has some implications for this work. Figure 2 has been computed at a constant supersaturation and one particle size. For practical reasons, the simulations in this work regard batch type operation of the reactor. In this type of operation, the supersaturation will be (partly) consumed by the growth of the particles. Since β_0 is only available at one supersaturation level, the simulations will intrinsically be performed under so-called chemostatic conditions. Also, although a small size-dependence is predicted in Mumtaz et al. (1997), only size-independent agglomeration is considered for now. A final, minor, simplification regarding the kinetic relation is the assumption that once particles have cemented together, they will never break apart again, even if higher shear rates are encountered than the ones present at collision. This assumption is plausible, since the collision time-scale is much smaller than the eddy lifetime, that is, the time for turbulence to alter its structure. This means that it will take a long time, compared to the chemical time-scales, before an agglomerate will enter a different shear regime. The agglomerate will therefore have a relatively long time to gain a strong bond. See Appendix A for a more elaborate discussion on this issue.

For applying the agglomeration kinetics proposed by Mumtaz et al. in CFD, some issues need to be resolved. Next, a description of the CFD-technique used is given, and the modeling strategy regarding particle transport is addressed. The implementation of the agglomeration kinetics is described. Since the kinetics are derived from a 2-D flow, a conversion step is needed to make it applicable for 3-D turbulent flows. Two types of conversion are investigated, and the theoretical background of these conversions is discussed.

Flow simulation and particle transport

It is the aim of this article to study the effect of scale-up on the overall agglomeration performance of a reactor. Due to the strong coupling between the flow phenomena and the agglomeration mechanism, it is essential to have a detailed description of the flow field. In this study, a computer code based on the lattice-Boltzmann method is used for this purpose. Details on the code can be found in Derksen and Van den Akker (1999). The method is based on tracking a set of fictitious particle densities on a lattice. One can derive that, for a specific lattice topology and equilibrium distribution, the Navier-Stokes equations are recovered. Although the lB-scheme is in essence just a method for solving the Navier-Stokes equations, it has some distinct advantages over conventional techniques, such as finite volume methods. Due to the highly local character of the lB-scheme, it can be parallelized relatively easily. Also, the implementation of an

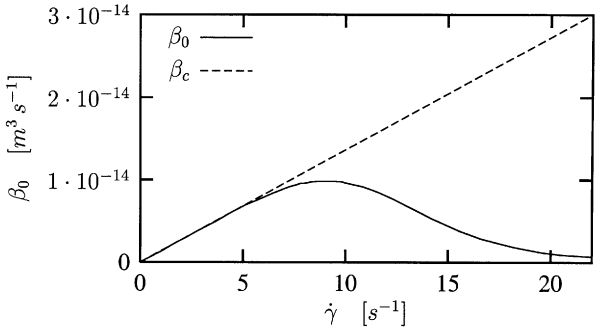

Figure 2. Kinetic relation for $CaOx \cdot H_2O$ agglomeration (Mumtaz et al.).

eddy-viscosity model to perform LES simulations can be handled very efficiently. It should be noted, however, that the proposed solution strategy for scalar transport and agglomeration is not restricted to an lB flow solver. In principle, any CFD package capable of doing LES can be implemented with this agglomeration model.

Since STRs are usually operated in the strongly turbulent regime, fully resolving the flow is practically impossible. Some sort of turbulence model has to be incorporated. Here, SGS fluctuations are incorporated by making use of a Smagorinsky model (Smagorinsky, 1963). The flowfield is decomposed in a resolved and an unresolved part. The large-scale flow structures are simulated directly (that is, large eddy simulation (LES)). No additional modeling is necessary here. The small-scale structures, with a size smaller than twice the grid-spacing, cannot be resolved by the grid. The net effect of these small-scale structures on the resolved field is incorporated by defining an artificial eddy viscosity. The flow equations for LES are obtained by applying a spatial filter to the continuity equation and the Navier-Stokes equations that will remove all small-scale fluctuations from the equations.

These filtered equations are given by:

$$\nabla \cdot \bar{\vec{v}} = 0 \tag{3a}$$

$$\frac{\partial \bar{\vec{v}}}{\partial t} + \nabla \cdot \left(\bar{\vec{v}} \bar{\vec{v}} \right) = -\frac{1}{\rho} \nabla p + \nu \nabla^2 \bar{\vec{v}} - \nabla \cdot \vec{\vec{\tau}}. \tag{3b}$$

The additional stress tensor $\vec{\vec{\tau}}$ represents the effect of the SGS motion on the resolved fluid-flow. This stress tensor is modeled by introducing an eddy viscosity ν_e

$$\vec{\vec{\tau}} = -\nu_e \left[\nabla \bar{\vec{v}} + \left(\nabla \bar{\vec{v}} \right)^T \right]. \tag{4}$$

In turn, this eddy viscosity is modeled (Smagorinsky, 1963)

$$\nu_e = c_s^2 \Delta^2 \sqrt{\bar{S}^2} \tag{5}$$

where the square of the resolved deformation rate $\bar{S}^2$ is defined as $(1/2)\,[\nabla \bar{\vec{v}} + (\nabla \bar{\vec{v}})^T] : [\nabla \bar{\vec{v}} + (\nabla \bar{\vec{v}})^T]$. The energy dissipation rate, an important parameter for modeling agglomera-

tion, is given by

$$\epsilon = (\nu_e + \nu)\bar{S}^2. \tag{6}$$

The implementation of the various geometries used (that is, baffled tank and impeller) is done by making use of a forcing algorithm (Derksen and Van den Akker, 1999). At a number of points, located at the surface of the geometry, the no-slip condition is enforced every time-step. This is done by checking the difference between the desired velocity (zero velocities at the static walls and the angular velocities at the moving walls), and the actual computed velocities. A force is applied to every point on the geometry to cancel this difference. This forcing method yields the desired geometry in the flow domain.

In the flow simulations, the liquid-solid flow is regarded as a pseudo one-phase system. This simplification can be justified by comparing the characteristic length- and time-scales of the particle and the flow. Assuming an aqueous system, 10 μm particles, a particle density of 2,000 kg·m^{-3} and a power input of 0.1 W kg^{-1} (an engineering rule of thumb that ensures that particles remain suspended), these scales are given by

$$\frac{d}{\lambda_k} \approx 0.2 \tag{7a}$$

$$\frac{1}{9}\frac{d^2}{\nu\tau_k} \approx 0.01 \tag{7b}$$

From Eq. 7a, it can be seen that the particles are smaller than the Kolmogorov length scale. Since the volume fraction and the particle-liquid density ratio are small, the particles will not significantly alter the structure of the turbulence. Equation 7b shows that the relaxation time of the particle is smaller than the smallest turbulent time-scale. As a consequence, the particles can easily keep up with any change in the flow. Therefore, the particles act as tracers, and the fluid may be considered as pseudo one-phase.

The fluid viscosity increases slightly due to the presence of particles. The size of this effect is estimated from Einstein's relation for suspension viscosity (Hiemenz, 1986)

$$\eta_o = \eta(1 + 2.5\phi) \tag{8}$$

where η_o is the effective dynamic viscosity of the suspension, η is the dynamic viscosity of the fluid, and ϕ is the particle volume fraction of the suspension. In this article, we use an initial particle number density of 10^{13} m^{-3}, with $d = 10^{-5}$ m. For this suspension $\phi = 5.23 \times 10^{-3}$, which means that the effective viscosity exceeds the fluid viscosity by 1.3% only. This effect is considered small enough to be neglected.

Gravitational effects are excluded and the validity of this simplification can be checked by comparing the additional particle slip velocity due to gravity with the characteristic fluid velocities. In principle, gravity can induce two types of particle motion: a mean- and a fluctuating slip velocity. The mean effect stems from the drag force needed to balance gravity, while the fluctuating effect results from a different fluctuating fluid velocity felt by the particle, due to its mean slip-velocity. Figure 3 shows these mechanisms. The characteristic velocity ratios are given by (see Appendix B)

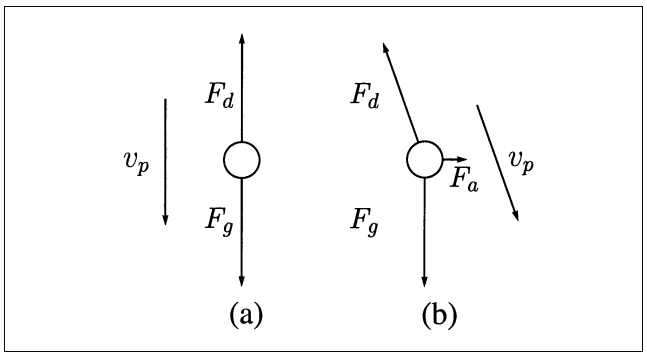

Figure 3. Influence of gravity on the particle velocity.

The mean effect is shown in (a), and the fluctuating effect in (b). Note that the fluctuating effect due to gravity may cause particle motion in a direction perpendicular to the gravity vector.

$$\frac{v_s}{U_m} = \frac{\tau_a g}{U_m}\left(\frac{\rho_p - \rho}{\rho_a}\right) \quad \text{for mean effects} \tag{9a}$$

$$\frac{v_s}{U_0} = \frac{\tau_a g}{U_0}\left(\frac{\rho_p - \rho}{\rho_a}\right) \quad \text{for fluctuating effects} \tag{9a}$$

The ratio $\tau_a g/U$ can be interpreted as the ratio of the particle Stokes (St) number to the Froude (Fr) number. If this ratio becomes small compared to unity, gravitational effects may be ignored. For the particles considered, $\tau_a = \mathcal{O}$ (10^{-5} s). Furthermore, $g \approx 10$ m·s^{-2}, and U_m as well as U_0 are $\mathcal{O}$ (1 m·s^{-1}) in the impeller region. Since $\tau_a q/U$ is in the range of 10^{-4}–10^{-3}, it is justified to exclude gravity. This reasoning does not take into account that the characteristic velocity in the bulk of an STR may be much smaller than the impeller tip speed. For low-velocity regions in the tank, the zero-gravity assumption may therefore break down. In practice, this means that particle setting may occur at very low impeller *Re* numbers. This effect cannot be resolved with our model at this stage.

Similarly to the gravitational effects, the fluid acceleration also leads to an additional slip-velocity of the particles. The ratios between the additional slip-velocity and the fluid characteristic-velocities are given by (see Appendix B)

$$\frac{\bar{v}_{sa}}{U_m} = \frac{\tau_a \bar{a}}{U_m}\left(\frac{3\rho}{2\rho_a}\right) \quad \text{for mean effects} \tag{10}$$

$$\frac{\bar{v}_{sa}}{U_0} = \frac{\tau_a \bar{a}}{U_0}\left(\frac{3\rho}{2\rho_a}\right) \quad \text{for fluctuating effects} \tag{11}$$

The mean fluid-acceleration can play an important role in flows with strong rotation. In the reactor, the highest values of the fluid acceleration occur near the tip of the impeller.

An upper-bound estimate of $\bar{a}$ can be obtained by

$$\bar{a}_{\max} \approx 2\frac{V_{\text{tip}}^2}{D_{\text{imp}}} \tag{12}$$

The values of $\bar{a}_{\max}$ depend on the size of the reactor, and in general is higher for smaller reactors. In most cases $\bar{a}_{\max}$ is of the same order or smaller than g. In a few cases $\bar{a}_{\max}$ is significantly higher than g. The highest value $\bar{a}_{\max} = 167\ \text{m}\cdot\text{s}^{-2}$ occurs in Case 1 (see Table 1). In Case 1 the value of $\tau_a \bar{a}/U$ is still small: in the range of 10^{-3}–10^{-2}. Therefore, in all the cases considered, it is justified to exclude fluid-acceleration effects on the particle motion.

Based on these arguments, the particles are assumed to move with the fluid velocity. The particle-number flux is calculated using the resolved velocities of the LES simulation. In principle, both the resolved (grid) and the nonresolved (subgrid) fluid motion contribute to the particle-number flux. However, it is also shown that the contribution of the subgrid-scale fluid motion can be neglected. The subgrid fluid-motion is important in determining the agglomeration rate, but not in determining the particle-number flux.

SGS intermittency, or the stochastic character of the turbulence energy dissipation rate ϵ at the SGS level, is not incorporated in this work. In the bulk region of the reactor, the resolution of the simulation is high enough to resolve almost all scales of turbulence. The SGS contribution, including intermittency, should therefore be small. In the impeller region, SGS intermittency may play a role, but ϵ levels are so high that agglomeration is unlikely to take place there. Incorporation of SGS intermittency is therefore consider to be "finetuning" and is postponed for future studies.

Conversion of 2-D to 3-D kinetics

Crude Model. From Eqs. 7a and 7b, it can be seen that the particles only experience the smallest turbulent scales directly. Dimensional analysis suggests that the deformation rate found at these scales is given by

$$\sqrt{S^2} \approx \dot{\gamma} \propto \sqrt{\frac{\epsilon}{\nu}}\ . \tag{13}$$

Crudely speaking, the deformation rate can be coupled to a shear rate, as is indicated in Eq. 13. As the energy dissipation rate is known locally from the flow simulations, a local shear rate can be computed. From the relation expressed in Figure 2, a local value for β_0 can be obtained. It should be kept in mind that since turbulence is essentially 3-D, $\dot{\gamma}$ also has a 3-D nature.

Some remarks on this modeling strategy have to be made. Principally, S^2, β_c and β_0 all depend on the value of the eigenvalues of the deformation rate. In contrast with 2-D flows, for 3-D flows, the relation between them is flow-dependent. For 3-D flows, $\dot{\gamma}$ should be considered as an effective value to be used in conjunction with the model by Mumtaz et al.

Equation 13 shows the need for a proportionality constant. Saffman and Turner (1956) investigated the collisions of iner-

Table 1. Numerical Setup*

	Const.	Vol. (m^3)	D_{imp} (m)	N ($\text{rev}\cdot s^{-1}$)	Re	$\bar{\epsilon}$ ($m^2\cdot\text{s}^{-3}$)	V_{tip} ($m\cdot s^{-1}$)	Imp. Type	Model	Res.
B	Re	10^{-1}	1.68×10^{-1}	7.11×10^{-1}	2×10^{4}	2.39×10^{-3}	3.75×10^{-1}	RT	c/r	120^3
1	Re	10^{-3}	3.61×10^{-2}	1.53×10^{1}	2×10^{4}	1.11	1.74	RT	c	120^3
2	Re	10^{-2}	7.78×10^{-2}	3.30	2×10^{4}	5.14×10^{-2}	8.07×10^{-1}	RT	c/r	120^3
3	Re	1	3.61×10^{-1}	1.53×10^{-1}	2×10^{4}	1.11×10^{-4}	1.74×10^{-1}	RT	c/r	120^3
4	Re	10^{1}	7.78×10^{-1}	3.30×10^{-2}	2×10^{4}	5.14×10^{-6}	8.07×10^{-2}	RT	c/r	120^3
5	$\bar{\epsilon}$	10^{-3}	3.61×10^{-2}	1.98	2.6×10^{3}	2.39×10^{-3}	2.25×10^{-1}	RT	c/r	120^3
6	$\bar{\epsilon}$	10^{-2}	7.78×10^{-2}	1.19	7.2×10^{3}	2.39×10^{-3}	2.90×10^{-1}	RT	c/r	120^3
7	$\bar{\epsilon}$	1	3.61×10^{-1}	4.27×10^{-1}	5.6×10^{4}	2.39×10^{-3}	4.84×10^{-1}	RT	c/r	120^3
8	$\bar{\epsilon}$	1	3.61×10^{-1}	4.27×10^{-1}	5.6×10^{4}	2.39×10^{-3}	4.84×10^{-1}	RT	r	180^3
9	$\bar{\epsilon}$	10^{1}	7.78×10^{-1}	2.56×10^{-1}	1.6×10^{5}	2.39×10^{-3}	6.25×10^{-1}	RT	c/r	180^3
10	v_{tip}	10^{-3}	3.61×10^{-2}	3.30	4.3×10^{3}	1.11×10^{-2}	3.75×10^{-1}	RT	c	120^3
11	v_{tip}	10^{-2}	7.78×10^{-2}	1.53	9.3×10^{3}	5.14×10^{-3}	3.75×10^{-1}	RT	c	120^3
12	v_{tip}	1	3.61×10^{-1}	3.3×10^{-1}	4.3×10^{4}	1.11×10^{-3}	3.75×10^{-1}	RT	c	120^3
13	Re	10^{-2}	7.78×10^{-2}	3.30	2×10^{4}	1.34×10^{-2}	8.07×10^{-1}	PBT	r	120^3
14	Re	10^{-1}	1.68×10^{-1}	7.11×10^{-1}	2×10^{4}	6.49×10^{-4}	3.75×10^{-1}	PBT	r	120^3
15	Re	1	3.61×10^{-1}	1.53×10^{-1}	2×10^{4}	3.01×10^{-5}	1.74×10^{-1}	PBT	r	120^3
16	Re	10^{1}	7.78×10^{-1}	3.30×10^{-2}	2×10^{4}	1.40×10^{-6}	8.07×10^{-2}	PBT	r	120^3
17	$\bar{\epsilon}$	10^{-3}	3.61×10^{-2}	3.06	4.0×10^{3}	2.39×10^{-3}	3.47×10^{-1}	PBT	r	120^3
18	$\bar{\epsilon}$	10^{-2}	7.78×10^{-2}	1.83	1.1×10^{4}	2.39×10^{-3}	4.48×10^{-1}	PBT	r	120^3
19	$\bar{\epsilon}$	10^{-1}	1.68×10^{-1}	1.10	3.1×10^{4}	2.39×10^{-3}	5.79×10^{-1}	PBT	r	120^3
20	$\bar{\epsilon}$	1	3.61×10^{-1}	6.58×10^{-1}	8.6×10^{4}	2.39×10^{-3}	7.47×10^{-1}	PBT	r	120^3
21	$\bar{\epsilon}$	1	3.61×10^{-1}	6.58×10^{-1}	8.6×10^{4}	2.39×10^{-3}	7.47×10^{-1}	PBT	r	180^3
22	$\bar{\epsilon}$	10^{1}	7.78×10^{-1}	3.95×10^{-1}	2.4×10^{5}	2.39×10^{-3}	9.65×10^{-1}	PBT	r	180^3
23	v_{tip}	10^{-3}	3.61×10^{-2}	3.30	4.3×10^{3}	3.02×10^{-3}	3.75×10^{-1}	PBT	r	120^3
24	v_{tip}	10^{-2}	7.78×10^{-2}	1.53	9.3×10^{3}	1.40×10^{-3}	3.75×10^{-1}	PBT	r	120^3
25	v_{tip}	1	3.61×10^{-1}	3.3×10^{-1}	4.3×10^{4}	3.02×10^{-4}	3.75×10^{-1}	PBT	r	120^3

*For the calculation of the specific power input, Po = 5 for the RT and Po = 1.36 for the PBT is assumed.

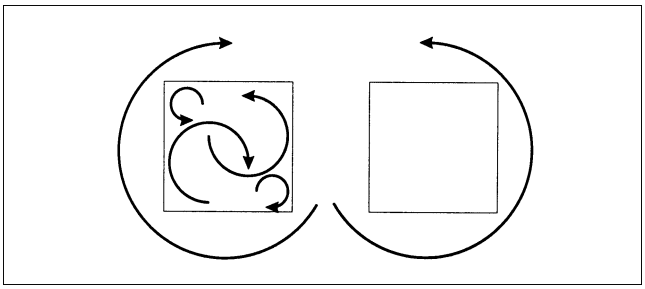

Figure 4. Relative importance of SGS motion in the impeller and the bulk region.

The squares represent a computational cell. In the impeller region (left), both large-scale and small-scale motion are present. The unresolved motion is modeled by the eddy-viscosity model. In the bulk region (right), no significant small-scale motion is found. The SGS contribution will therefore be small.

tia-less droplets. They derived a constant of approximately 1.29 for the case of homogeneous isotropic turbulence and monodisperse particles (note that the constant is 4/3 for monodisperse particles in 2-D shear flow). However, the flow in a stirred vessel is clearly not homogeneous and isotropic. For the lack of a better estimate of the proportionality constant, the constant was set to 4/3.

Another problem arises from the large differences in turbulent scales between the impeller swept region and the bulk region in the vessel (Figure 4). Near the impeller where most of the turbulence is generated, dissipation rates can be orders of magnitude larger than the average dissipation rate. In the bulk part of the vessel, turbulence levels are much lower, which results in larger values for the Kolmogorov length scale. For the LES-simulations performed in this article, this means that in the impeller region, the SGS contribution will be large, whereas in the bulk region the SGS contribution will be small (that is, in the bulk part of the vessel, we practically have a direct numerical simulation (DNS)).

As was mentioned earlier, the energy dissipation rate is calculated using $\epsilon = (\nu + \nu_e)\bar{S}^2$. This implies that the resolved part of the dissipation rate will be lumped into the estimate of Eq. 13. As will be outlined next, strictly speaking, this is not valid.

Due to the above-mentioned issues, this type of modeling will from now on be referred to as the "crude model."

Refined Model. The modeling errors mentioned above can be largely overcome by using the collision rate model proposed by Mei and Hu (1999). They studied the collisions of inertia-less particles in turbulent flows with a mean shear. In that article, the collision rate is derived from the eigenvalues of the rate of strain tensor, thereby taking into account the possibly anisotropic nature of the turbulent flow. Their model converges to the collision model by Von Smoluchowski for a 2-D laminar case, and to the model by Saffman and Turner for homogeneous isotropic turbulence. Mei and Hu also incorporated the effect of a mean shear rate on the collision rate. This concept is used in this article to take into account the contribution of grid scale (GS) and SGS collisions properly.

Mei and Hu derived a relation for the number of collisions in a turbulent flow with a mean velocity gradient, where the coefficients are fitted for a rapidly sheared homogeneous turbulent flow

$$\beta_c \approx d^3\sqrt{\frac{\epsilon}{\nu}}\left\{1.2944^{2.2} + \left[\frac{1.33\dot{\gamma}}{\sqrt{\frac{\epsilon}{\nu}}}\right]^{2.2}\right\}^{1/2.2} \tag{14}$$

for monodisperse particles. The first term in Eq. 14 describes the collision due to homogeneous turbulence, whereas the second term takes into account the collision contribution due to mean shear. This relation is the result of a fit through data obtained from numerical simulations of a rapidly sheared homogeneous turbulent flow.

For the refined algorithm presented here, the total energy dissipation rate is decomposed into a GS and a SGS contribution. By definition

$$\epsilon = \nu\overline{S^2} = \nu\overline{\left(\bar{S} + S'\right)^2} = \nu\bar{S}^2 + \nu\overline{S'^2}. \tag{15}$$

From the definition of the eddy-viscosity ν_e, one can derive that

$$\nu_e\bar{S}^2 = \nu\overline{S'^2} = \epsilon_{SGS}. \tag{16}$$

It is therefore valid to decompose the GS and SGS dissipation rate into

$$\epsilon = \nu_t\bar{S}^2 = (\nu + \nu_e)\bar{S}^2 \Rightarrow \tag{17a}$$

$$\epsilon_{GS} = \nu\bar{S}^2 \tag{17b}$$

$$\epsilon_{SGS} = \nu_e\bar{S}^2. \tag{17c}$$

With this decomposition, it is possible to use Eq. 14 in a consistent way. The SGS dissipation rate is obtained by means of the Smagorinsky model and is therefore modeled under the assumption of isotropic turbulence on the small scales. This ϵ_{SGS} can therefore be used for the terms involving $\sqrt{\epsilon/\nu}$ in Eq. 14. For the resolved part of the flow, the assumption of isotropy is not needed, since all flow information is known at these scales. Following the same approximation as shown earlier, $\sqrt{\bar{S}^2}$ is used as an estimate for the mean shear (that is, the $\dot{\gamma}$) contribution in Eq. 14. As mentioned before, it should be noted that $\dot{\gamma}$ has a 3-D nature. Strictly speaking, $\sqrt{\bar{S}^2} = \dot{\gamma}$ is valid only for 2-D flows. For 3-D flows, a more rigorous approach would require the use of the eigenvalues of S. These 3-D effects will result in a different "effective value" for $\dot{\gamma}$. However, we do not expect these effects to be very important, since the proportionality constant for 3-D homogeneous isotropic turbulence is not very different from the constant for 2-D laminar shear flow (see Eq. 14).

The agglomeration rate constant β_0 is now derived from the relation between the collision rate constant and the agglomeration rate constant given by Figure 2. The computed 3-D collision rate constant is matched to the 2-D collision

rate constant for a planar shear flow. At this β_c, the model by Mumtaz et al. predicts an accompanying β_0. This β_0 is assumed to be the agglomeration rate constant for the refined model. This procedure effectively means that only the collision efficiency proposed by Mumtaz et al. has to be used.

The relation between $\beta_c = 4/3\ \dot{\gamma} d^3$ and β_0 is approximated by a parametric fit through the curve in Figure 2. The fit is given by

$$\beta_0 \approx 1.209\beta_c \exp\left(-8.30\times10^{-3}\beta_c^2 + 1.09\times10^{-1}\beta_c - 0.514\right). \tag{18}$$

It is useful to explain why a relatively sophisticated model is used for determining the collision rate, but the agglomeration rate constant (that is, the collision efficiency) is still based on kinetics obtained in 2-D flow. The main reason is that, to the authors' knowledge, 3-D kinetics are not available. This means that, at this point, this is the best model that exists. It is expected the conversion step will not be in great error. Mumtaz et al. integrated over various collision angles to obtain the kinetic relation. The treatment of SGS collisions is consistent with this method: SGS turbulence is assumed to be isotropic, which means that no preferential collision direction is present. The agglomeration rate constant at the SGS level may therefore be assumed to be equal to the "angle-mean" value from Figure 2. Furthermore, it is observed that only a small difference in proportionality constants exists between collisions due to homogeneous isotropic turbulence and collisions due to a mean velocity gradient (see Eq. 14). This seems to indicate that the influence of the flow phenomena is not very different for the two collision mechanisms. This suggests that, for the collision efficiency, the differences between the two mechanisms will also be small.

Equation 14 is valid for a rapidly sheared homogeneous turbulent flow only, and not for any flow. However, Eq. 14 contains separate contributions for the shear part and the homogeneous isotropic turbulence part. Since these two contributions are not very different, it is reasonable to expect Eq. 14 to give adequate results in more general situations. In fact, Eq. 14 also suggests that the "crude model" should yield results not very different from the approach described here. The model described will be referred to as the "refined model."

Implementation of the Agglomeration Reaction. Agglomeration is assumed to be size-independent. The agglomeration rate is implemented by solving a transport equation for the particle-number concentration m_0 on the same LES grid of the fluid–flow simulation.

The reaction rate is determined by the local agglomeration rate and the local particle-number concentration. The local agglomeration-rate constant is computed from the local flow conditions, using either the crude or the refined model, described previously. The reaction rate is given by

$$r = -\frac{1}{2}\beta_0 m_0^2. \tag{19}$$

Based on the arguments discussed previously, and presented in detail in Appendix B, the particles are assumed to move with the fluid velocity. The general form of the transport equation for the particle-number concentration m_0 can be written as

$$\frac{\partial m_0}{\partial t} + \nabla\cdot\vec{J} = r \tag{20}$$

where $\vec{J}$ is the particle-number flux. In principle, both the resolved (grid) and the nonresolved (subgrid) fluid motion can contribute to the resolved particle-number concentration m_0. The subgrid contribution to the reaction rate r is taken into account in either the crude or the refined models, described previously. In the following we show the subgrid contribution to the particle-number flux can be neglected.

The particle-number flux can be decomposed into a resolved (grid) and a nonresolved (subgrid) part:

$$\vec{J} = \vec{J}_g + \vec{J}_s. \tag{21}$$

The resolved particle-number flux is given by

$$\vec{J}_g = \vec{U}_g m_0 \tag{22}$$

where $\vec{U}_g$ is the resolved fluid-velocity. Therefore, for incompressible flow

$$\nabla\cdot\vec{J}_g = \vec{U}_g\cdot\nabla m_0. \tag{23}$$

The subgrid particle-number flux can be estimated using a subgrid diffusivity D_s

$$\vec{J}_s = D_s\nabla m_0 \tag{24}$$

$$\nabla\cdot\vec{J}_s = D_s\nabla^2 m_0. \tag{25}$$

An upperbound estimate of D_s is given by

$$D_s \approx U'_{s0}\Delta \tag{26}$$

where U'_{s0} is a characteristic-value of the subgrid fluid-velocity fluctuations, and Δ is the grid spacing. Therefore, an upperbound estimate for the ratio between the divergence of the subgrid and resolved particle-number fluxes is given by

$$\left|\frac{\nabla\cdot\vec{J}_s}{\nabla\cdot\vec{J}_g}\right|_{\max} \approx \frac{U'_{s0}}{U_{g0}}\frac{\Delta}{L_c} \tag{27}$$

where U_{g0} is a characteristic-value of the resolved fluid-velocity, and L_c is a characteristic-value of the resolved particle-number concentration length-scale. The ratio between U'_{s0} and U_{g0} can be estimated through the usual isotropic local-equilibrium mixing-length reasoning (Eggels, 1994; Mason

and Callen, 1986)

$$\frac{U'_{s0}}{U_{g0}} \approx C_s \frac{\Delta}{L_h} \tag{28}$$

where L_h is a characteristic-value of the resolved hydrodynamic length-scale, and C_s is the value of the Smagorinsky coefficient used in the SGS model ($C_s \approx 0.1$). Combining Eqs. 27 and 28 one gets

$$\left|\frac{\nabla\cdot\vec{J}_s}{\nabla\cdot\vec{J}_g}\right|_{\max} \approx C_s \frac{L_h}{L_c}\left(\frac{\Delta}{L_h}\right)^2. \tag{29}$$

The agglomeration is determined by the flow strain-rate, and the time required for agglomeration is much smaller than the resolved hydrodynamic time-scale (the time required for agglomeration is of the order of the Kolmogorov time-scale $\sqrt{\nu/\epsilon}$). Therefore, assuming a local equilibrium between turbulence production and dissipation, one gets

$$L_c \approx L_h. \tag{30}$$

Combining Eqs. 29 and 30 gives an upperbound estimate for the ratio between the divergence of the subgrid and resolved particle-number fluxes

$$\left|\frac{\nabla\cdot\vec{J}_s}{\nabla\cdot\vec{J}_g}\right|_{\max} \approx C_s\left(\frac{\Delta}{L_h}\right)^2. \tag{31}$$

The value of Δ/L_h depends on the LES resolution. At least one has $\Delta/L_h < 1/2$, and smaller values for higher resolutions. Assuming a coarse resolution with $\Delta/L_h \approx 1/3$ and $C_s \approx 0.1$, one gets

$$\left|\frac{\nabla\cdot\vec{J}_s}{\nabla\cdot\vec{J}_g}\right|_{\max} \approx 10^{-2}$$

being even smaller for an higher-resolution LES. Therefore, it is justified to neglect the contribution of the subgrid fluid-motion to the particle-number flux.

The above estimates were confirmed by Hollander et al. (2000), who used a "discrete eddy concept" (Sommerfeld et al., 1993) to model the subgrid particle motion. They found the differences in the simulations with and without subgrid particle motion to be negligible (of the order of 1%).

In this article the contribution of the subgrid fluid motion to the particle-number flux is neglected. The transport equation for the particle-number concentration reduces to

$$\frac{\partial m_0}{\partial t} + \nabla\cdot\left(\vec{U}_g m_0\right) = r \tag{32}$$

where the resolved fluid-velocity $\vec{U}_g$ is supplied by the LES of the fluid flow.

Numerical Setup

Simulation details

A standard stirred vessel was used, equipped with four baffles with a width of $D_{\text{tank}}/10$. The vessel height H was equal to D_{tank}. At the top, a free surface was mimicked with a free slip wall. The impellers used were a standard 6-blade Rushton Turbine (RT) and a 4-blade pitched blade turbine (PBT). The simulations were performed on a $120\times120\times120$ grid, except for simulations with an impeller Re-number $> 10^5$. For these simulations, a $180\times180\times180$ grid was used. The flow conditions were imposed by fixing N, D, and ν in the lB code. Properties like the Re-number and the impeller tip speed were fixed this way. The specific power input arises from the flow simulation.

Figure 5a shows the RT geometry, while the PBT geometry, taken from Schäfer et al. (1998), is presented in Figure 5b. Both impellers had a diameter of $D_{\text{tank}}/3$ and bottom clearance of $D_{\text{tank}}/3$. In the simulations, the blades have zero thickness. The impeller shaft is not incorporated in the simulations. Zero blade thickness is not an intrinsic limitation of the forcing algorithm applied here, but it is imposed by a

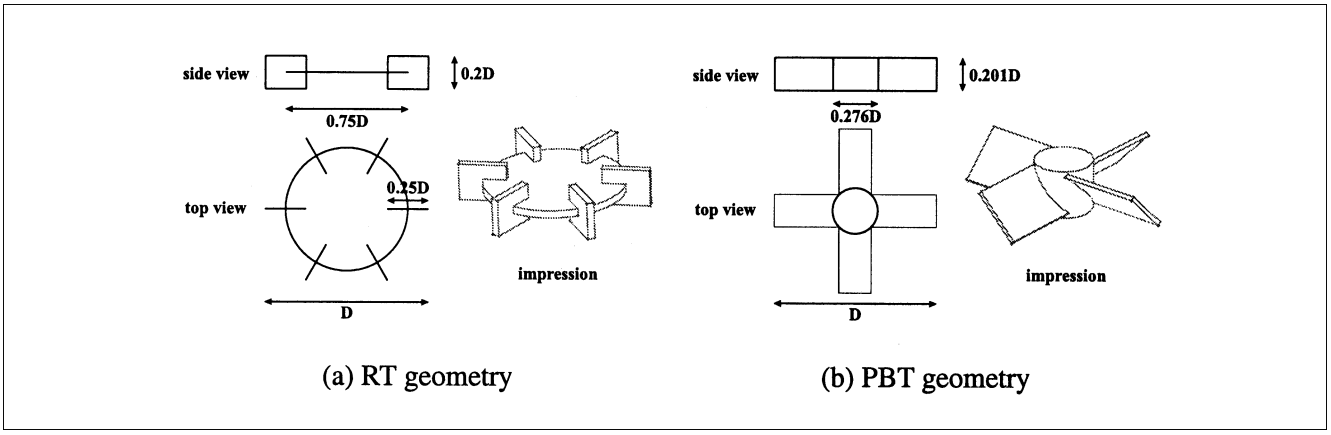

Figure 5. Definition of impeller geometries.

practical limitation on the computational efforts that could be handled. To give an impeller blade a thickness comparable to practical situations, a computational domain of at least 180^3 is needed. Our resources did not allow for such an effort. It was therefore decided to do most of the runs on a lower resolution (120^3) with thin impeller blades. The drawback of this approach is the flow is resolved less accurately. Global flow tests indicated, for instance, that the Po-number based on the integrated energy dissipation rate, was too low by up to a factor of 2. In Derksen and Van den Akker (1999) the Po-number based on the torque of the impeller and that based on the total dissipation rate in the vessel were in good agreement, indicating consistency. Comparison between angle-resolved LDA-data and the simulated flow fields also showed good agreement. Therefore it is believed that the computer code for the flow-field simulation is accurate within the limits proposed by the Smagorinsky model and the numerical resolution that could be used. In spite of the limitations mentioned, the flow simulations may be sufficiently accurate to obtain insight in agglomeration behavior and trends.

For all simulations, a fully developed flowfield is used as an initial condition. The simulations were run for 10 impeller revolutions. Although the simulations were started with an initially homogeneous particle concentration field, the particle concentration becomes inhomogeneously distributed, due to the local nature of β_0. To be able to compare the results of different runs, the run time in terms of impeller revolutions was kept constant.

Interpretation of the results

A procedure adopted from physical agglomeration experiments is used to interpret the simulation results. Every time step, the average number concentration in the entire reactor is computed. Through these data the rate law for size-independent agglomeration is fitted

$$\frac{dm_0}{dt} = -\frac{1}{2}\hat{\beta}_0 m_0^2 \Rightarrow m_0(t) = \frac{1}{1/2\,\hat{\beta}_0 t + 1/m_{00}} \qquad (33)$$

This procedure results in an observed (reactor averaged) $\hat{\beta}_0$. This rate constant is the combined result of kinetics and hydrodynamic conditions, just like in real-life experiments. It gives an appropriate measure for comparing reactors with different scale, impeller type and operating conditions.

Since the basis of the simulations are LES flow-field calculations, in principle, one would need to perform statistics on the numerical results. This would mean that the runs should be repeated several times to obtain a proper estimate for $\hat{\beta}_0$. At this stage, the computational demands for such a procedure are too large. As a test, two cases were run twice, using different starting flow fields, to see the difference in the observed agglomeration rate constant. The differences were within 1%. Therefore it was assumed that one run per case would give sufficient insight in the reactor performance.

The agglomeration results were linked to the specific power input determined from the assumed *Po* number (that is, 5 for the RT and 1.36 for the PBT), rather than to the simulated *Po* number for the various cases. We believe that this method is closest to the experimental procedure in physical experiments: in practice, the specific power input is usually not measured, but a tabulated value is assumed.

Scale-up rules

Three scale-up rules common to chemical engineering are investigated: constant *Re* number, constant impeller tip speed, and constant specific power input. Scale-up at constant *Re* number implies the same overall hydrodynamics at varying reactor sizes, while scale-up at constant v_{tip}, common in bioengineering applications, is used if a certain constraint on the velocity is required. Finally, scale-up at constant specific power input gives a constant number of collisions at all scales, if particle collisions only (that is, no agglomeration) would be considered. An additional scaling rule that might be of interest is scale-up at constant rotational speed. This way, the macroscopic mixing time could be kept constant. The computational demands do not allow for investigating this rule yet, since the *Re*-number for a large vessel would become very large [$\mathcal{O}(2\times10^6)$].

Computational demands

The simulations were performed on a cluster of 12 PIII/500MHz processors, with 500 MB of RAM per CPU and Linux as an operating system. Typical memory requirements were 400 MB for the 120^3 grid-node simulations and 1.4 GB for the 180^3 grid-node simulations. Typical execution times were 2.5 days on 2 CPU's for the 120^3 cases and 8.5 days on 3 CPU's for the 180^3 cases.

Results

General flow field results

In Figure 6, some typical simulations results are depicted for cases "B" (refined) and "14" (see Table 1). Both cases are for a 100 L vessel, at a *Re* number of 20,000. The results shown relate to a vertical plane midway between the baffles. The lefthand part of each figure has always been obtained by averaging the results over 10 impeller revolutions, while the righthand parts show instantaneous realizations.

Figures 6a and 6b show the flowfields generated by the RT and the PBT, respectively. The averaged results show the well-known dual-circulation pattern for the RT and the single-circulation pattern for the PBT. The difference in macroscopic flow structure allows for a critical test on the relative importance of macro-scale mixing. The instantaneous vector fields indicate the presence of the trailing vortices near the impeller tips. Also, meso-scale coherent structures can be observed that migrate through the vessel. These structures are responsible for local differences in hydrodynamic conditions and, therefore, have a pronounced effect on the local agglomeration rate.

In Figures 6c and 6d, $\sqrt{\epsilon/\bar{\epsilon}}$ is shown for the two impeller types. The color-coding is on a log-scale. This quantity can be seen as a relative measure of the collision rate-constant β_c in the tank, since it scales with $\sqrt{\epsilon/\nu}$ (at least for the crude model). While β_c is large in the impeller region, it is small in the bulk region. The instantaneous values again show variations due to the presence of the coherent structures. Care should be taken while comparing the RT and the PBT results. Since the simulations are performed at equal *Re* num-

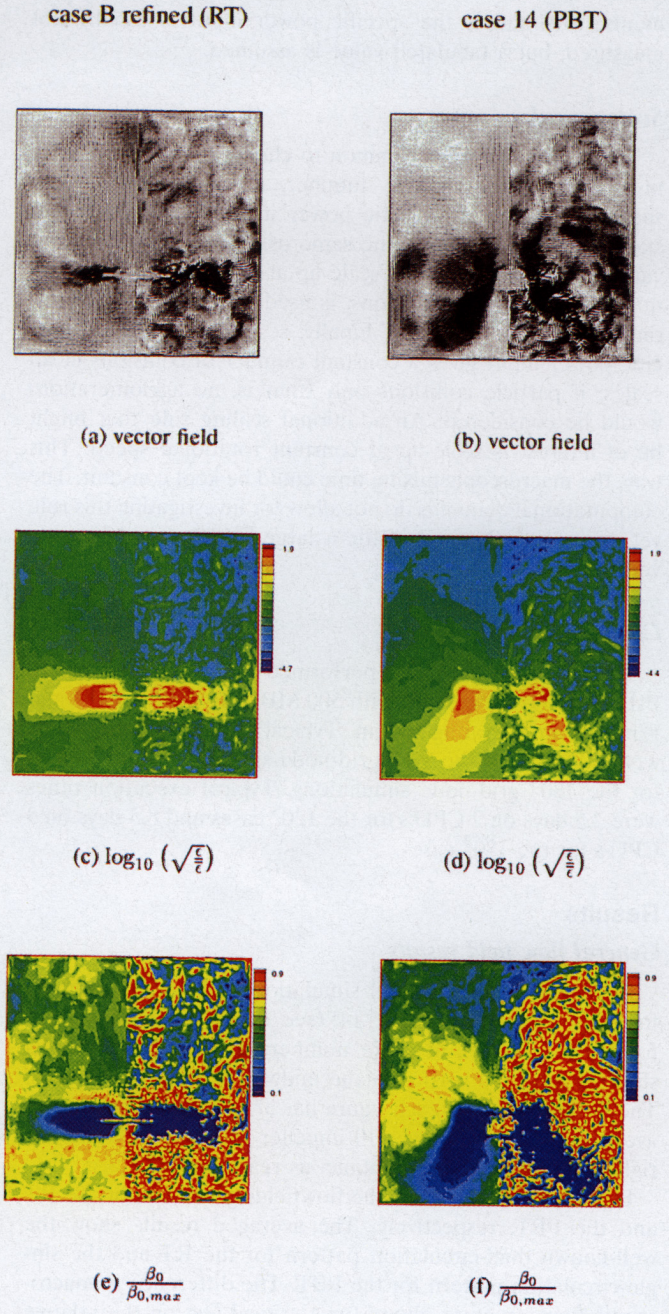

Figure 6. Global flow field features.

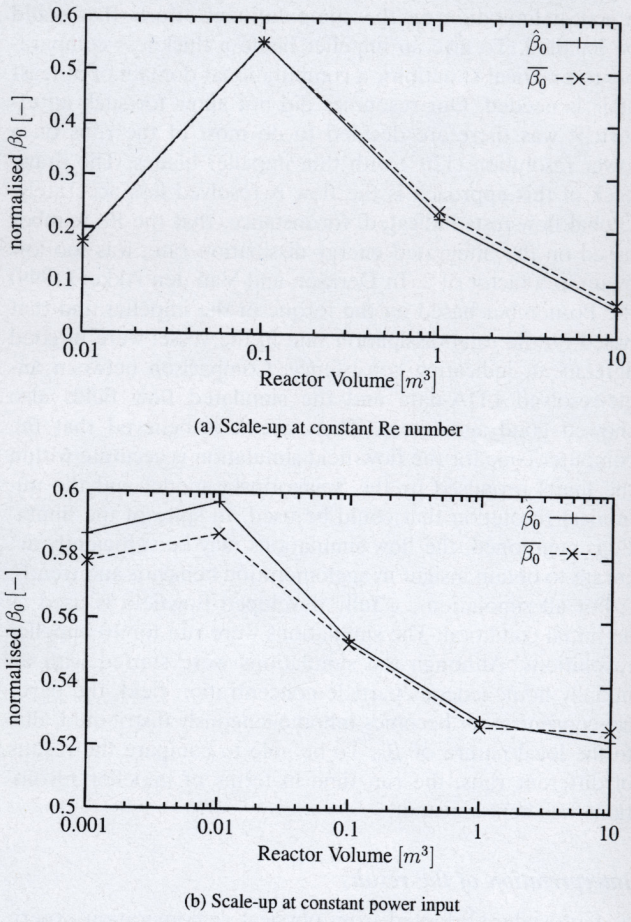

Figure 7. Comparison of $\hat{\beta}_0$ and $\overline{\beta_0}$ for an RT.

Results are obtained from the refined model simulations. The agglomeration rate-constant is normalized by the maximum value of β_0 in Figure 2.

bers, while the Po number is different for the impellers, the specific power input is different for the two cases. This picture is meant only to demonstrate how β_c varies.

Figures 6e and 6f show the normalized agglomeration rate constant. It is interesting to see that in the impeller region, where β_c is high, β_0 is almost zero. The fact that β_0 is a highly nonlinear function of $\sqrt{\epsilon/\nu}$ results in large gradients in the local and instantaneous values of β_0. A striking difference between the RT and PBT results is the position and size of a relatively high β_0 zone. For the RT case, this zone seems to be restricted to the lower recirculation loop, while for the PBT case the zone takes up a significant part of the bulk region.

Along with β_0, the particle concentration needs to be known for calculating the agglomeration rate. As a result of the agglomeration process itself, however, the total particle concentration decreases in time. An indirect measure for the degree of variation in particle concentration follows from comparing $\hat{\beta}_0$ and $\overline{\beta_0}$, where the former is the agglomeration rate constant estimated from the particle number decay in time, and the latter is obtained by averaging the local β_0 over the reactor volume. Note that $\hat{\beta}_0$ also contains information on particle transport effects and thus incorporates the possible effects of an uneven distribution of particles. If the particles are distributed homogeneously over the tank, these two quantities should be equal.

In Figure 7, the difference between $\hat{\beta}_0$ and $\overline{\beta_0}$ is plotted for the RT. All agglomeration rate constants have been normalized with the maximum value of the Mumtaz-curve in Figure 2. Figure 7a shows the effect of scale-up on $\hat{\beta}_0$ and $\overline{\beta_0}$ at constant *Re*-number. For small reactor volumes, $\hat{\beta}_0$ and $\overline{\beta_0}$ are virtually identical, whereas for larger sizes, the two quantities start diverging. This may be due to inhomogeneous particle distribution at larger vessel sizes. The macroscopic hy-

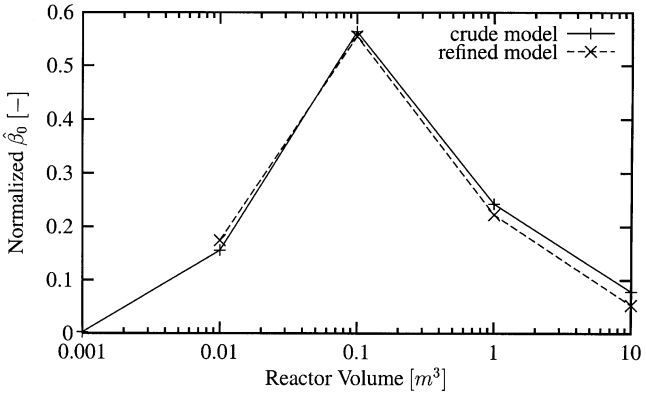

Figure 8. Comparison between crude and refined model.

Scale-up at constant *Re* number, for a Rushton Turbine.

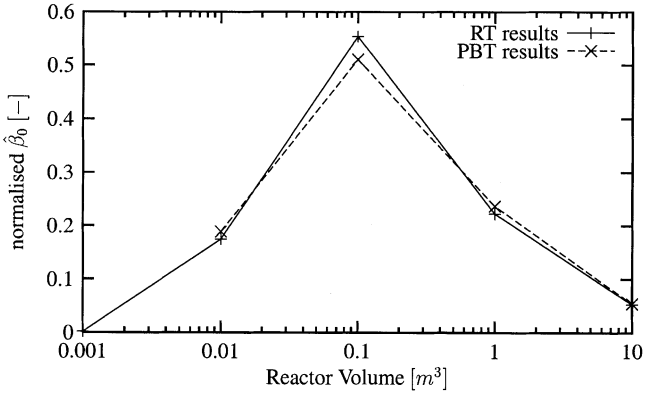

Figure 9. Numerical scale-up at constant *Re* number for a RT and a PBT.

drodynamic time-scale $1/N$ increases at scale-up, while the chemical time-scale $1/\beta_0 m_0$ remains constant (see Appendix A). Therefore, the reactor may develop macroscale inhomogeneities at increasing reactor size. An interesting effect can be observed with scale-up at constant power input (see Figure 7b). In small reactors, the observed agglomeration rate constant is higher than $\overline{\beta_0}$, while at large scales, $\hat{\beta}_0$ is smaller. Note that the macromixing time-scale varies for these simulations. A situation in which $\hat{\beta}_0$ is large than $\overline{\beta_0}$ occurs if particle concentration and the agglomeration rate constant are positively correlated. The reverse effect (that is, $\overline{\beta_0}$ larger than $\hat{\beta}_0$) can occur if, on average, high concentrations are encountered with low β_0 and vice versa.

Comparison crude and refined model

The difference in using either the crude or refined model, as described earlier, is shown in Figure 8 for scale-up at constant *Re*-number. It can be seen that for the refined model, $\hat{\beta}_0$ seems to be shifted towards a somewhat lower shear rate in the Mumtaz-curve (Figure 2). This can be explained as follows: for large reactor volumes, the average shear-rate is low. On average, the agglomeration rate constant is taken from the lefthand (linear) part of Figure 2. Here, the refined model yields a lower estimate for $\hat{\beta}_0$ than the crude model, indicating a situation with a lower effective shear rate. At small reactor volumes, the average shear rate is high and the agglomeration rate constant is mainly taken from the righthand (decreasing) part of Figure 2. Here, the refined model predicts a higher reactor efficiency than the crude model, which is also an indication for a situation with a lower effective shear rate. This is consistent with the pre-factor for $\sqrt{\epsilon/\nu}$ in the model of Mei and Hu (1999) being smaller than 4/3. The differences between the two models are small, as expected. However, the refined model may physically be more correct. Since the extra numerical effort is minor, most simulations were performed with the refined model.

Scale-up results

Constant Re-Number, RT and PBT. In Figure 9, the reactor performance as a function of reactor volume for scale-up at constant *Re*-number is presented for both RT and PBT. Note that the 1 L case for the PBT was not simulated to save computational efforts. The $\hat{\beta}_0$ for this case is expected to be very close to zero, like with the RT case. For both impeller types, a maximum in $\hat{\beta}_0$ is observed for a reactor volume of 100 L. This is caused by a decreasing average shear rate at increasing reactor volume. At small reactor volumes, agglomeration according to the righthand side of the Mumtaz curve prevails, whereas at large volumes, the lefthand side of this curve is dominant. It is striking that for both impeller geometries $\hat{\beta}_0$ is almost equal, while the specific power input for these impellers differs by more than a factor of 3. This could partly be caused by the resolution issue described earlier.

Constant Power-Input, RT and PBT. RT and PBT show quite different behavior for scale-up at constant specific power input (Figure 10; note that the scale of the y-axis is different from the previous plots). In general, the agglomeration rate constant decreases at increasing reactor volume for the RT, while it increases for a PBT. In addition, the PBT cases yield much lower values for $\hat{\beta}_0$ than the RT. The differences observed may be related to particle concentration inhomogeneities. The local flow conditions, and, therefore, the agglomeration rate constant, are highly nonuniform. As a

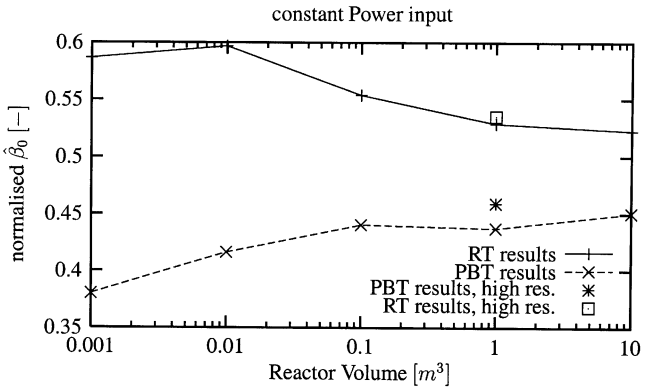

Figure 10. Numerical scale-up at constant specific power input for a RT and a PBT.

consequence, the number concentration shows a large decrease in particular regions in the vessel, whereas, at other points, the concentration remains constant. Since the hydrodynamic time-scale is much larger than the agglomeration time-scale responsible for the gradients, large inhomogeneities in particle concentration may sustain (see Appendix A). This effect is somewhat counterintuitive, as, usually, turbulence reduces concentration gradients. In this case, however, turbulence induces gradients in agglomeration rates, and, therefore, in particle number concentration.

The simulations for 1,000 L were performed at both 120^3 and 180^3 grid-node resolution. This was done to get insight into the sensitivity of the results to numerical resolution. A difference of about 10% could be found. Some effects contribute to this difference. First, the refined model used for this comparison is slightly sensitive to the relative contributions of GS and SGS turbulence, which may depend on numerical resolution. Second, the overall flowfield is captured in more detail when higher resolutions are used. At this point, one of the drawbacks of the present implementation of the lB-scheme becomes evident. As all simulations were performed on uniform grids, the resolution in the impeller region is relatively low, compared to that in the bulk region, since smaller turbulent structures are present near the impeller than in the bulk. By use of a uniform grid, the flow is resolved to a higher extent in the bulk than near the impeller. Increasing the numerical resolution of a simulation, therefore, affects the degree of detail near the impeller and, as a result, the macroscopic flow field. Finally, the Smagorinsky SGS model is known to fail in describing the effects at the SGS accurately.

Constant v_{tip} RT and PBT. The effect of scale-up at constant v_{tip} on reactor performance is substantial (see Figure 11), although the shape of the curves for the RT and PBT is rather similar. Again, the PBT gives a lower agglomeration rate than the RT. To limit computational efforts, the 10,000 L cases have not been simulated.

The results for scale-up at constant v_{tip} are in between the results for scale-up at constant *Re*-number and power-input. At least qualitatively, this can be explained by investigating the powers of N and D for the various scale-up rules. They are ND^2, N^3D^2 and ND for constant *Re*-number, power input, and tip speed, respectively. Realizing that keeping ND constant also means that N^2D^2 is constant, shows that at constant D the power of N for constant tip speed lies in between the power of N for constant *Re*-number and power input.

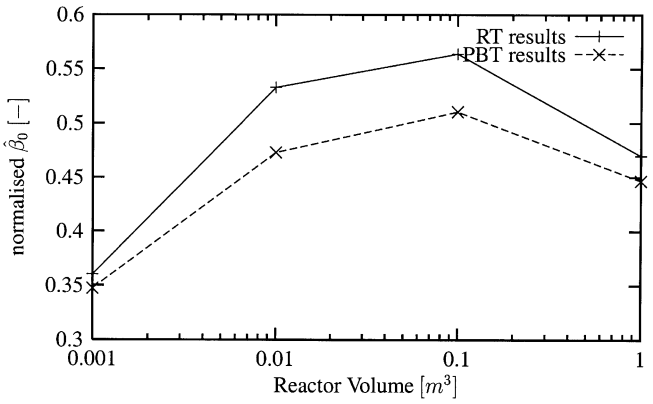

Figure 11. Numerical scale-up at constant v_{tip}, for a RT and a PBT.

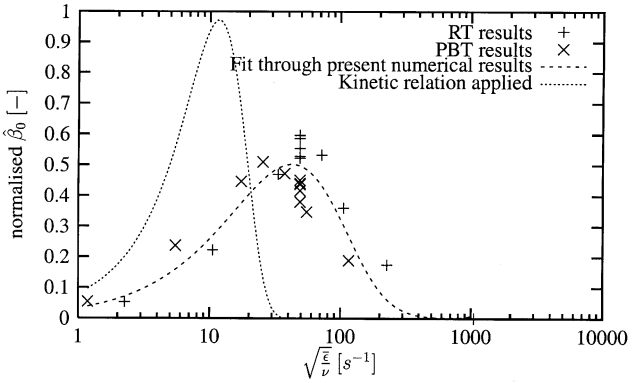

Figure 12. Applied kinetic relation vs. kinetics derived from simulation results.

Comparison with Standard Interpretation. In Figure 12, all simulation results have been plotted against $\sqrt{\bar{\epsilon}/\nu}$. This method is frequently used in experimental work to derive kinetic relations. Also, the kinetic relation applied is shown. The scatter in the results is large, and the maximum β_0 is found to be too low, as well as at too high a shear rate, at least compared to the kinetic relation applied. Statistics are much better than in experimental work, here. The scatter in real data sets will therefore be much larger. However, even in this case, the reconstruction of the original kinetics seems virtually impossible. This emphasizes that oversimplifying the flow conditions in a reactor may lead to poor estimates of agglomeration kinetics.

A final comment can be made on the kinetic relation used here. At this stage, no proper validation for Figure 2 is found in literature. To the authors' knowledge, only two articles (Hollander et al., 1998; Mumtaz et al., 1998) have attempted to reconstruct this curve experimentally. The main criticism about this curve was that it predicts an optimum shear rate for agglomeration that is much smaller than the average shear rates found in common STR experiments. Figure 12 shows, however, that the optimum shear rate for $\hat{\beta}_0$ is found at a much higher shear rate than would be expected from the kinetic relation. The simulation results indicate that, due to flow interactions, the observed optimum for β_0 is shifted towards more plausible values for this average shear rate. This might be an indication that Figure 2 is actually closer to reality than one might expect at first hand.

Conclusions

Effects of scale-up on reactor agglomeration performance numerically were investigated numerically. The results indicate that the influence of hydrodynamics on agglomeration is larger and more complex than is usually assumed. Local hydrodynamic conditions cause a large spread in the local agglomeration rate constant. Also, the nonuniform distribution of particles in the reactor has a profound effect on the effective agglomeration rate in the reactor. One of the more dra-

matic effects on agglomerator performance is the influence of impeller geometry. Only taking into account the Po-number of an impeller fails to explain the observed differences in agglomeration behavior between a RT and a PBT.

Two methods for converting the 2-D agglomeration kinetics proposed by Mumtaz et al. to the 3-D turbulence as encountered in a STR were tested. In the crude method, local values for ϵ are converted to an equivalent 2-D shear rate, which in turn is used to determine a local β_0. The refined model properly accounts for agglomeration due to velocity gradients at the resolved flow scales. The differences between the results obtained with the two methods were small for the conditions simulated. We believe that the refined model presented in this work is physically more correct. Since the increase in computational effort is only minor, the refined model is preferred over the crude model.

Some caution should be taken using these simulation results to reinterpret experimental data. In this study, the initial particle concentration is relatively high (10^{13} m^{-3}). This concentration was primarily chosen to increase the overall reaction rate and, therefore, limit the computational times needed (at slower reaction rates, the number of impeller revolutions needed to properly estimate $\hat{\beta}_0$ increases). It might be tempting to rescale the presented results to different concentrations, by making use of, for example, the characteristic reaction time-scale $1/\hat{\beta}_0 m_{00}$. This approach, however, affects the ratio of the hydrodynamic time scales and the chemical time scales as well. As a result of the various nonlinear interactions mentioned in the article, a completely different system is obtained.

One of the major assumptions in our approach is that the agglomeration process is taking place at constant supersaturation, that is, in a chemostatic environment. The reason for this is that no kinetic relation is available for β_0 as a function of shear rate *and* local supersaturation. In experimental work, the supersaturation usually decreases in time. As a consequence, the differences in agglomeration behavior of the different flow systems observed in our simulations may become stronger if the effect of the time evolution of the supersaturation is taken into account.

Some numerical issues regarding the results presented are worth mentioning. The total simulation time for this article was about 1 CPU-year. To obtain real grid-independence, computational domains of 180^3 or larger are needed, which would mean an increase of at least a factor of 5 for computational resources. This was not feasible at this stage. However, the results in this article do show that the agglomeration mechanism is very sensitive to small-scale flow phenomena and that high-resolution simulations are therefore necessary. Increasing the numerical resolution would decrease the SGS model contribution and therefore give better results. Higher resolutions would also allow for a more detailed description of the impeller geometry. This study leaves some major numerical issues unresolved. The method does give insight in the trends in reactor performance, however. It is the authors' opinion that this type of simulations may contribute to better reactor design in the near future.

A final difference between these simulations and common practical conditions for agglomeration is the fact that the simulations are performed at relatively low $\bar{\epsilon}$. The reason for this is in the practical limitations to the numerical simulations. Increasing dissipation rates imply increasing Reynolds numbers, and therefore increasing computational demands. It has been shown, however, that the technique is applicable for doing scale-up studies.

Acknowledgment

The authors would like to acknowledge Prof. G. M. Van Rosmalen for her scientific input on modeling the agglomeration process. Also, the DIOC-programme M3 is acknowledged for funding this research.

Notation

d = particle diameter, m
d_1, d_2 = diameter of particle 1, 2, m
D = impeller diameter, m
D_{tank} = tank diameter, m
F_a, F_d, F_g = acceleration, drag, gravity force, kg·m·s^{-2}
g = gravitational acceleration constant, m·s^{-2}
H = tank height, m
k = turbulent kinetic energy, m^2·s^{-2}
L = characteristic length, m
m_0 = zeroth moment of the PSD, m^{-3}
N = impeller rotational speed, rev·s^{-1}
N_1, N_2 = particle number density of size 1,2, m^{-3}
p = pressure, kg·m^{-1}·s^{-2}
P = total power input, kg·m^2·s^{-3}
r_{12} = agglomeration rate, m^{-3}·s^{-1}
$\bar{S}^2$ = square of resolved deformation rate, s^{-2}
t_A, t_H = agglomeration, hydrodynamic timescale, s
T_f = characteristic hydrodynamic timescale, s
$\bar{u}, u'$ = mean, fluctuating fluid velocity, m·s^{-1}
U_0, U_m = characteristic turbulent, mean velocity scale, m·s^{-1}
$\bar{v}, v'$ = mean fluctuating particle velocity, m·s^{-1}
v_p = particle velocity, m·s^{-1}
$\bar{v}_s, v'_s$ = mean, fluctuating slip velocity, m·s^{-1}
v_{tip} = impeller tip speed, m·s^{-1}

Greek letters

β_0 = agglomeration kernel, m^3·s^{-1}
$\overline{\beta_0}, \hat{\beta}_0$ = volume averaged, observed agglomeration kernel, m^3·s^{-1}
β_c = collision kernel, m^3·s^{-1}
$\dot{\gamma}$ = shear rate, s^{-1}
ϵ = energy dissipation rate, m^2·s^{-3}
$\bar{\epsilon}$ = volume averaged energy dissipation rate, m^2·s^{-3}
$\epsilon_{GS}, \epsilon_{SGS}$ = Grid Scale, Sub-Grid Scale dissipation rate, m^2·s^{-3}
η_o, η = observed, standard fluid viscosity, kg m^{-1}s^{-1}
λ_k = Kolmogorov length scale, m
ν, ν_e, ν_t = fluid, eddy, total viscosity, m^2·s^{-1}
τ_a = particle relaxation time, s
τ_k = Kolmogorov timescale, s
ρ, ρ_a, ρ_p = fluid, added mass, particle density, kg·m^{-3}
ϕ = volume fraction

Dim. numbers

Fr = Froude number, U_m^2/gL
Po = power number, $P/(\rho N^3 D^5)$
Re = Reynolds number, ND^2/ν
St = Stokes number, $(\tau_a U_m)/L$

Literature Cited

Bramley, A., M. Hounslow, and R. Ryall, "Aggregation during Precipitation from Solution. Kinetics for Calcium Oxalate Mono Hydrate," *Chemical Eng. Sci.*, **52**, 747 (1997).

Collier, A., and M. Hounslow, "Growth and Aggregation Rate for Calcite and Calcium Oxalate Monohydrate," *AIChE J.*, **45**(11), 2298 (1999).

Derksen, J., and H. van den Akker, "Large Eddy Simulations on the Flow Driven by a Rushton Turbine," *AIChE J.*, **45** (2), 209 (1999).

Eggels, J., "Direct and Large Eddy Simulation of Turbulent Flow in a Cylindrical Pipe Geometry," PhD Thesis, Laboratory for Aero- and Hydrodynamics, Delft University of Technology, The Netherlands (1994).
Hiemenz, P. C., *Principles of Colloid and Surface Chemistry*, 2nd ed, Marcel Dekker, New York (1986).
Hollander E. D., J. J. Derksen, O. S. L. Bruinsma, H. E. A. van den Akker, and G. M. van Rosmalen "A Numerical Study on the Coupling of Hydrodynamics and Orthokinetic Agglomeration," *Chem. Eng. Sci.* **56**, 2531 (2001).
Hollander, E., J. Derksen, O. Bruinsma, and H. Van den Akker, "Measuring the Effect of Hydrodynamics on Agglomeration," *Proc. of 1998 Annual AIChE Meeting*, Miami, 156 (1998).
Hollander, E., O. Bruinsma, J. Derksen, G. van Rosmalen, and H. van den Akker, "A Numerical Investigation into the Influence of Mixing on Orthokinetic Agglomeration," *10th European Conf. on Mixing*, Delft (2000).
Leeuwen V. M., "Precipitation and Mixing," PhD Thesis, Laboratory for Process Equipment, Delft University of Technology, The Netherlands (1998).
Mason, P., and Callen, N., "On the Magnitude of the Subgrid-Scale Eddy Coefficient in Large-Eddy Simulations of Turbulent Channel Flow," *J. Fluid Mech*., **162**, 439 (1986).
Maxey, M., and J. Riley, "Equation of Motion for a Small Rigid Sphere in a Nonuniform Flow," *Phys. Fluids A*, **26**, 883 (1983).
Mei, R., and K. Hu, "On the Collision Rate of Small Particles in Turbulent Flows," *J. Fluid Mech*., **391**, 67 (1999).
Mumtaz, H., M. Hounslow, N. Seaton, and W. Paterson, "Orthokinetic Aggregation during Precipitation: A Computational Model for Calcium Oxalate Monohydrate," *Trans. IChemE*, **75**, 152 (1997).
Mumtaz, H., N. Seaton, and M. Hounslow, "Towards a Priori Prediction of Aggregation Rates during Crystallization," *Proc. of 1998 Annual AIChE Meeting*, Miami (1998).
Randolph, A., and M. Larson, *Theory of Particulate Processes, Analysis and Techniques of Continuous Crystallization*, Academic Press, New York and London (1971).
Saffman, P., and J. Turner, "On the Collision of Drops in Turbulent Clouds," *J. Fluid Mech*., **1**, 16 (1956).
Schäfer, M., M. Yianneskis, P. Wächter, and F. Durst, "Trailing Vortices Around a 45° Pitched-Blade Impeller," *AIChE J*., **44**, 1233 (1998).
Smagorinsky, J., "General Circulation Experiments with the Primitive Equations: 1. The Basic Experiment," *Mon. Weather Rev*., **91**, 99 (1963).
Sommerfeld, M., G. Kohnen, and M. Rüger, "Some Open Questions and Inconsistencies of Lagrangian Particle Dispersion Models," *Ninth Symp. on "Turbulent Shear Flow,"* Kyoto, Japan, 15.1.1 (1993).
Ten Cate, A., S. Bermingham, J. Derksen and H. Kramer, "Compartmental Modeling of an 1,100L DTB Crystallizer Based on Large Eddy Flow Simulation," *10th European Conf. on Mixing*, 255 (2000).
Van Leeuwen, M., C. Huizer, O. Bruinsma, M. Hounslow, and G. Van Rosmalen, "The Influence of Hydrodynamics on Agglomeration of Aluminum Hydroxide: An Experimental Study," *Int. Conf. on Mixing and Crystallization* (1998).
Von Smoluchowski, M., "Versuch einer mathematischen theorie der Koagulationskinetik Koloider Lösungen," *Z. Phys. Chem*., **92**, 156 (1917).
Zauner, R., and A. G. Jones, "Scale-up of Continuous and Semi-batch Precipitation Processes," *Ind. Eng. Chem. Res*., **39**, 2392 (2000).

Appendix A: Comparison of Time Scales

Comparing the various chemical and hydrodynamic timescales in the agglomeration process can provide insight in the relative importance of the mechanisms in play. On a macroscopic (reactor) level, the hydrodynamic time scale is given by $1/N$. This time scale describes, for example, the time needed for large-scale particle transport. The characteristic macroscopic chemical time scale is given by $1/\beta_0 m_0$. Defining the ratio of these time scales

$$\frac{t_H}{t_A} = \frac{\beta_0 m_0}{N} \tag{A1}$$

When this ratio $\ll 1$, the reaction rate is expected to be homogeneous on a macroscopic scale, while a ratio $\gg 1$ indicates that gradients on a reactor level may occur. From this reasoning, it can be seen that at increasing reactor sizes, the degree of large-scale inhomogeneity will increase.

On a microscopic level, the particle contact time describes the amount of time primary particles have to cement together. For a 2-D shear flow, the time can be estimated to be $[1/2(d_1 + d_2)]/[1/2(d_1 + d_2)\dot{\gamma}] \propto \sqrt{\nu/\epsilon}$. The hydrodynamic time scale on the microscale is given by $1/\dot{\gamma} = \sqrt{\nu/\epsilon}$. The ratio of these time scales is 1 by definition. This indicates that at the microscopic level, agglomeration and fluid flow are strongly coupled. From this relation, it is still unknown whether the collision will be effective or not. This must be derived from a chemical time scale, that will involve the growth rate of the material. This is essentially what has been done by Mumtaz et al. and is described by the kinetic relation in Figure 2.

Usually, hydrodynamic effects can be neglected if the macroscopic chemical time scale is large compared to the macroscopic hydrodynamic time scale. This seems to be the case for standard agglomeration reactions [$(\beta_0 m_0)/N$ is usually around 10^{-2}]. However, in agglomeration, the microscopic time sale is of more importance. In this case, the time for species A to change to species B (that is, primary particles to change to an agglomerate) is dominant. This explains the strong coupling between agglomeration and fluid flow.

On a mesoscopic level, variations in agglomeration rate due to a distribution in turbulence levels can be captured. The chemical time scale is still given by $\sqrt{\nu/\epsilon}$, but the hydrodynamic time scale is now the characteristic time for the turbulence to alter its structure, that is, the eddy lifetime k/ϵ. The ratio of these time scales is given by

$$\frac{t_H}{t_A} = \frac{k}{\sqrt{\nu\epsilon}} = \frac{k}{v_k^2}. \tag{A2}$$

For typical conditions in stirred vessels, this ratio is $\mathcal{O}(100)$, which indicates that agglomeration can easily keep up with the changes in turbulence. This observation has two implications. First the local agglomeration rate constant can be based on the local and instantaneous flowfield. It is not necessary to take into account the hydrodynamic history of a particle. Secondly, it is unlikely that a particle will rupture after a successful agglomeration event, even if it is convected from a low-shear region to a high-shear region. The reason for this is that Eq. A2 shows that an agglomerate experiences typically 100 "growth-times," before it is subjected to a significantly different shear rate. In this time, the bond between the primary particles has become increasingly strong (typically 100^2 times stronger, due to the fact that a contact area is being built). The viscous force acting on an agglomerate can be estimated to be $\propto \eta d^2 \dot{\gamma} \propto \sqrt{\epsilon/\nu}$. If the energy dissipation rate would therefore increase four orders of magnitude

in one large eddy lifetime, the viscous forces would still only increase 100 times. Accordingly, this would not be enough to break the bond of the agglomerate.

Appendix B: Gravitational and Fluid-Acceleration Effects on the Particle Motion

In this Appendix the influence of the gravity and fluid-acceleration on the equation of motion of the particles is analyzed. A criterion is derived to evaluate the importance of gravitational and fluid-acceleration effects, on the mean and fluctuation values of the particle velocity.

For small particles (significantly smaller than the smallest length-scale of the flow), with a particle Reynolds number much smaller than one, the lift and Basset forces can be neglected, and the drag force can be assumed to be Stokes drag (Maxey and Riley, 1983). Considering Stokes drag, the gravity force, the surrounding-fluid stress, and the added mass, the equation of motion for a small particle is given by

$$\rho_p \frac{\pi d_p^3}{6}\frac{d\vec{v}}{dt} = \underbrace{3\pi\eta d_p(\vec{u}-\vec{v})}_{\text{drag}} + \underbrace{\rho_p \frac{\pi d_p^3}{6}\vec{g}}_{\text{gravity}} + \underbrace{\frac{\pi d_p^3}{6}\left(\nabla\cdot\vec{\vec{T}}\right)}_{\text{stress}} + \underbrace{\frac{\rho}{2}\frac{\pi d_p^3}{6}\left(\frac{D\vec{u}}{Dt}-\frac{d\vec{v}}{dt}\right)}_{\text{added mass}} \tag{B3}$$

where $\vec{u}$ and $D\vec{u}/Dt$ are, respectively, the velocity and acceleration of the surrounding fluid, and $\nabla\cdot\vec{\vec{T}}$ is the surface-force per unit of volume acting on the surrounding fluid ($\vec{\vec{T}}$ is the fluid stress-tensor). Neglecting the influence of the particles on the fluid, the acceleration of the surrounding fluid is given by

$$\vec{a} \equiv \frac{D\vec{u}}{Dt} \equiv \frac{\partial\vec{u}}{\partial t} + (\nabla\vec{u})\cdot\vec{u} = \frac{1}{\rho}\left(\nabla\cdot\vec{\vec{T}}\right) + \vec{g}. \tag{B4}$$

Combining Eqs. B3 and B4, one obtains

$$\frac{d\vec{v}}{dt} = \frac{1}{\tau_a}(\vec{u}-\vec{v}) + \left(\frac{\rho_p-\rho}{\rho_a}\right)\vec{g} + \left(\frac{3\rho}{2\rho_a}\right)\vec{a} \tag{B5}$$

where ρ_a and τ_a are defined as

$$\rho_a \equiv \rho_p + \frac{\rho}{2}$$

$$\tau_a \equiv \frac{\rho_a d_p^2}{18\eta}$$

Equation B5 states that the particle acceleration depends on the particle slip-velocity (that is, the difference between the velocities of the particle and the surrounding fluid), the acceleration of gravity, and the acceleration of the surrounding fluid. Equation B5 can be decomposed into a mean (ensemble averaged) and a fluctuating part

$$\frac{d\bar{\vec{v}}}{dt} = -\frac{1}{\tau_a}\bar{\vec{v}}_s + \left(\frac{\rho_p-\rho}{\rho_a}\right)\vec{g} + \left(\frac{3\rho}{2\rho_a}\right)\bar{\vec{a}} \tag{B6}$$

$$\frac{d\vec{v}'}{dt} = -\frac{1}{\tau_a}\vec{v}_s' + \left(\frac{3\rho}{2\rho_a}\right)\vec{a}' \tag{B7}$$

where the mean and fluctuating parts of the particle slip-velocity are defined as

$$\bar{\vec{v}}_s \equiv \bar{\vec{v}} - \bar{\vec{u}}$$

$$\vec{v}_s' \equiv \vec{v}' - \vec{u}'.$$

Note that the ensemble average is made on the particles, with $\vec{u}$ and $\vec{a}$ being the velocity and acceleration of the surrounding fluid, respectively.

Equation B6 states the average particle-acceleration is due to: the average slip velocity, the acceleration of gravity, and the average acceleration of the surrounding fluid. In some situations the acceleration of the surrounding fluid can play an important role; such as, in flows with strong rotation. Equation B6 can be rewritten as

$$\frac{\bar{\vec{v}}_s}{U_m} = -\frac{\tau_a}{U_m}\frac{d\bar{\vec{v}}}{dt} + \frac{\bar{\vec{v}}_{sg}}{U_m} + \frac{\bar{\vec{v}}_{sa}}{U_m} \tag{B8}$$

where U_m is a characteristic mean-velocity of the fluid, and $\bar{\vec{v}}_{sg}$ and $\bar{\vec{v}}_{sa}$ are defined as

$$\bar{\vec{v}}_{sg} \equiv \tau_a\vec{g}\left(\frac{\rho_p-\rho}{\rho_a}\right)$$

$$\bar{\vec{v}}_{sa} \equiv \tau_a\bar{\vec{a}}\left(\frac{3\rho}{2\rho_a}\right).$$

Clearly, the gravitational and fluid-acceleration effects produce an additional slip velocity. The importance of the gravitational mean slip velocity, compared to the mean fluid velocity in the reactor, is given by

$$\frac{\bar{v}_{sg}}{U_m} = \frac{\tau_a g}{U_m}\left(\frac{\rho_p-\rho}{\rho_a}\right) \tag{B9}$$

and the influence of the gravity on the mean particle velocity can be neglected if $\bar{v}_{sg}/U_m \ll 1$.

Similarly, the importance of the fluid-acceleration mean slip velocity, compared to the mean fluid velocity in the reactor, is given by

$$\frac{\bar{v}_{sa}}{U_m} = \frac{\tau_a\bar{a}}{U_m}\left(\frac{3\rho}{2\rho_a}\right) \tag{B10}$$

and the influence of the mean fluid-acceleration on the mean particle velocity can be neglected if $\bar{v}_{sa}/U_m \ll 1$.

Equation B7 states the particle-acceleration fluctuation is due to the fluctuations in the slip-velocity and surrounding-

fluid acceleration. To estimate the importance of gravity on the particle-velocity fluctuation, one has to estimate the differences in the fluctuations of the surrounding-fluid velocity and acceleration, with and without gravity. In the absence of gravity, the values of $\vec{u}'$ and $\vec{a}'$ can be characterized by a turbulence fluid velocity U_0 and a turbulence fluid acceleration A_0. If gravity is present, additional fluctuations in the fluid velocity and fluid acceleration are experienced by the particle. This is caused by the fact that the particles move through an eddy with an extra slip-velocity $\bar{\vec{v}}_{sg}$. An estimate of the additional fluctuations in the surrounding-fluid velocity and acceleration, $\vec{u}'_{sg}$ and $\vec{a}'_{sg}$, can be obtained from

$$\frac{d\vec{u}'_{sg}}{dt} \approx \bar{\vec{v}}_{sg} \cdot \nabla \vec{u}'$$

$$\frac{d\vec{a}'_{sg}}{dt} \approx \bar{\vec{v}}_{sg} \cdot \nabla \vec{a}'.$$

Since $\nabla \vec{u}' \approx U_0/L$, $\nabla \vec{a}' \approx A_0/L$, and $T_f \approx L/U_0$, one obtains

$$u'_{sg} \approx \bar{v}_{sg} \frac{U_0}{L} T_f \approx \bar{v}_{sg}$$

$$a'_{sg} \approx \bar{v}_{sg} \frac{A_0}{L} T_f \approx \frac{\bar{v}_{sg}}{U_0} A_0.$$

The additional fluctuations in the surrounding-fluid velocity and acceleration, due to gravitational effects, are given by

$$\frac{u'_{sg}}{U_0} \approx \frac{\bar{v}_{sg}}{U_0} = \frac{\tau_a g}{U_0} \left(\frac{\rho_p - \rho}{\rho_a} \right) \tag{B11}$$

$$\frac{a'_{sg}}{A_0} \approx \frac{\bar{v}_{sg}}{U_0} = \frac{\tau_a g}{U_0} \left(\frac{\rho_p - \rho}{\rho_a} \right). \tag{B12}$$

Clearly, the influence of the gravity on the particle-velocity fluctuation can be neglected if $\bar{v}_{sg}/U_0 \ll 1$.

Similarly, the additional fluctuations in the surrounding-fluid velocity and acceleration, due to the mean fluid-acceleration, are given by

$$\frac{u'_{sa}}{U_0} \approx \frac{\bar{v}_{sa}}{U_0} = \frac{\tau_a \bar{a}}{U_0} \left(\frac{3\rho}{2\rho_a} \right) \tag{B13}$$

$$\frac{a'_{sa}}{A_0} \approx \frac{\bar{v}_{sa}}{U_0} = \frac{\tau_a \bar{a}}{U_0} \left(\frac{3\rho}{2\rho_a} \right) \tag{B14}$$

and the influence of the mean fluid-acceleration on the particle-velocity fluctuation can be neglected if $\bar{v}_{sa}/U_0 \ll 1$.

Manuscript received Jan. 2, 2001, and revision received Mar. 26, 2001.